Biophysical Journal, Volume *113*

Supplemental Information

Lipid Order Degradation in Autoimmune Demyelination Probed by Polarized Coherent Raman Microscopy

Paulina Gasecka, Alexandre Jaouen, Fatma-Zohra Bioud, Hilton B. de Aguiar, Julien Duboisset, Patrick Ferrand, Herve Rigneault, Naveen K. Balla, Franck Debarbieux, and Sophie Brasselet

Lipid order degradation in autoimmune demyelination probed by polarization resolved coherent Raman microscopy Supporting Material

P. Gasecka, A. Jaouen, F.-Z. Bioud, H. B. de Aguiar, J. Duboisset, P. Ferrand, H. Rigneault, N. K. Balla, F. Debarbieux, and S. Brasselet

1 PR-CARS data analysis

The calculation of the CARS polarized (PR-CARS) response from the lipid assembly present in the focal volume of an objective relies on a bond additive model where individual CH molecular bonds add-up coherently to form a nonlinear susceptibility tensor γ for each vibration mode, responsible for the CARS nonlinear coherent radiation. These bond dipoles directions **e** with orientations (θ, φ) in the macroscopic frame form a macroscopic nonlinear susceptibility tensor $\chi^{(3)}_{IJKL}$ of the lipid assembly in the macroscopic 3D frame (X, Y, Z). It has been shown that since the incident optical field is polarized in the (X, Y) plane, the read-out of the CARS signal occurs from a reduced 2D macroscopic tensor (1):

$$\chi^{(3)}_{IJKL} = N\gamma \int_{\varphi} (\mathbf{I}\cdot\mathbf{e})(\mathbf{J}\cdot\mathbf{e})(\mathbf{K}\cdot\mathbf{e})(\mathbf{L}\cdot\mathbf{e})p(\varphi)d\varphi \tag{1}$$

where $(I, J, K, L) = (X, Y)$. N is the molecular bonds density, γ is the molecular vibration tensor norm, $(\mathbf{I}\cdot\mathbf{e})$ refers to the projection of the **e** vector on the macroscopic frame axis **I**, and $p(\varphi)$ is the orientational distribution function of **e** vectors averaged on their out-of plane orientation (θ) (1). The nonlinear response finally depends on the function $p(\varphi)$, a 2D effective distribution function that can be decomposed over its symmetry orders read by the PR-CARS process:

$$p(\varphi) = p_0 + p_2\cos(2\varphi) + q_2\sin(2\varphi) + p_4\cos(4\varphi) + q_4\sin(4\varphi) \tag{2}$$

where p_0 is the isotropic contribution to the angular distribution, (p_2, q_2) are its second order symmetry components and (p_4, q_4) its fourth order symmetry components. Relations between the macroscopic nonlinear susceptibility terms ($\chi^{(3)}_{XXXX}, \chi^{(3)}_{XXXY}$...) and the angular distribution function parameters ((p_2, q_2), ...) can be found in (1).

In the PR-CARS analysis, both incident pump field (E_p) and Stokes field (E_s) are linearly polarized and rotated with a variable angle α relative to the sample plane horizontal axis X. The CARS intensity can be written as (1):

$$I^{CARS}_{I}(\alpha) \quad \propto \quad \sum_{\substack{JKL \\ MNO}} \chi^{(3)}_{IJKL}\chi^{(3)*}_{IMNO}E_{p,J}E_{p,K}E^{*}_{s,L}E^{*}_{p,M}E^{*}_{p,N}E_{s,O}(\alpha). \tag{3}$$

where $E_{p,J}(\alpha)$ is the projection of the pump incident field on the axis **J** in the sample plane. In the PR-CARS data analysis, the total CARS intensity is decomposed on a circular basis:

$$\begin{aligned} I^{CARS}(\alpha) \quad \propto a_0 \quad & +a_2\cos(2\alpha) + b_2\sin(2\alpha) + a_4\cos(4\alpha) + b_4\sin(4\alpha) \\ & +a_6\cos(6\alpha) + b_6\sin(6\alpha), \end{aligned} \tag{4}$$

where the (a_n, b_n) coefficients are directly calculated from the recorded polarization dependent image stack by projection on circular basis functions.

The (p_n, q_n) parameters are deduced from these coefficients following the relations (1, 2):

$$\begin{aligned} a_0 &= \tfrac{1}{64}(36p_0^2 + 10p_2^2 + 10q_2^2 + p_4^2 + q_4^2) \\ a_2 &= \tfrac{1}{32}(24p_0p_2 + 3p_2p_4 + 3q_2q_4);\ b_2 = \tfrac{1}{32}(p_0q_2 + 3p_2q_4 - 3p_4q_2) \\ a_4 &= \tfrac{3}{32}(p_2^2 - q_2^2 + 2p_0p_4);\ b_4 = \tfrac{3}{16}(2p_0q_4 + p_2q_2) \\ a_6 &= \tfrac{1}{32}(p_2p_4 - q_2q_4);\ b_6 = \tfrac{1}{32}(p_2q_4 + p_4q_2) \end{aligned} \tag{5}$$

0006-3495/08/09/2624/12 $2.00

2 Sources of error and bias in PR-CARS measurements

Stringent control of the PR-CARS signal conditions are required in order to ensure the validity of the measured order parameters. In this part the different sources of error and bias are investigated.

2.1 Noise

First, S_2, S_4 values are only collected for high-enough intensity values, that guaranty sufficiently low bias and low noise (Fig. S1). Above 1300 analog signal value, standard deviations are of 0.02 for S_2 and 0.08 for S_4. This intensity value will be set as a threshold for all quantitative studies. Above this threshold, we also observe that the S_2 bias is negligible. Concerning S_4, the residual bias (which does not surpass 0.15 with the chosen intensities) is systematically removed from all measured values, accounting for the local pixel intensities and the reference noise-intensity dependence depicted (Fig. S1). In conclusion by using intensity thresholding, the measured parameters are relevant for statistical analysis and hence for comparison between different myelin regions and scores.

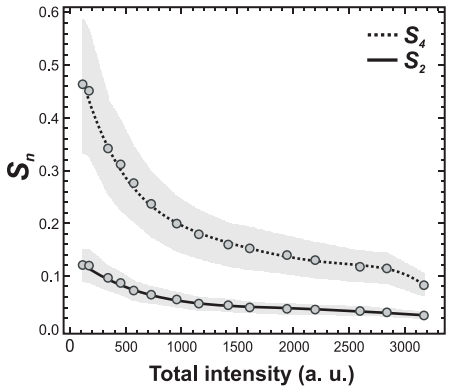

Figure S1: S_2 and S_4 dependence on the CARS intensity signal (summed over 18 input polarization angles) in the isotropic medium. The shaded region represents the standard deviation of the mean S_2 and S_4 values.

2.2 Non-resonant background

Second, some care has to be taken regarding the existence of non-resonant background in the data. Considering our previous studies performed on model multilamellar lipid membrane vesicles, it is obvious that the non-resonant Four Wave Mixing (FWM) signal can lead to an underestimation of S_2 (2). The difference between measured values and background-free ones (measured in absence of non-resonant background by Stimulated Raman Scattering (SRS)) have been estimated to be about 0.2 in multilamellar vesicles (MLVs) made of dipalmitoylphosphatidylcholine (DPPC), S_4 being almost un-affected (2). In this work we display raw data, however it is worth noting that the background-free S_2 values have to be increased by an offset, which is most probably not higher than 0.2, considering that MLVs data are very close to values measured in myelin (see below).

2.3 Out of plane mean orientation

Third, (S_2, S_4) values depend on possible out-of-plane orientations of the observed distributions. All the models developed in this work assume that the molecular angular distributions are lying in the sample plane. In order to properly report structural properties of myelinated axons, one needs to ensure that the PR-CARS measurement is performed at the equatorial plane of the axon/myelin tube. Any out-of-plane orientation of the observed distribution can indeed bias the results interpretation by adding a component which tends towards isotropy. In order to estimate how the (S_2, S_4) order parameters depend on this

effect in the myelin sheath, we performed PR-CARS measurements at several focusing planes (Z steps every 0.5 μm) crossing the whole 3D tubular structure of the myelin sheath from bottom to top (Fig. S2). S_2 seems to be robust with negligible

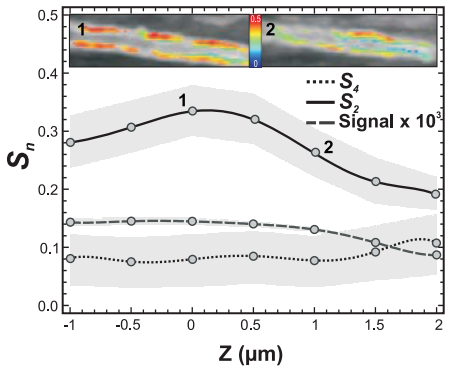

Figure S2: S_2 and S_4 mean values measured on a myelin sheath as a function of the sample depth Z. The shaded regions indicate the standard deviation of the order parameters (over all pixels in selected regions along the myelin sheath, according to an intensity thresholding of 75% of the maximum intensity measured in the image). Z$=0$ corresponds to the depth of the myelin tube equatorial plane. Insets: S_2 images after intensity thresholding, at Z$=0$ (point 1) and 1 μm above (point 2). Both images are superimposed with the CARS intensity images in grayscale.

modification over a defocus of ± 5 μm around the equatorial plane. This means that as long as the myelin sheath looks visually in focus (which is the case for this defocus range), the S_2 measurement is reliable. Moreover its standard deviation does not depend on Z. S_4 on the other hand is very robust to a defocus change, which is consistent with the fact that defocus changes the apparent disorder of the distribution, not its shape. The only noticeable changes of S_4 are a slight increase at the largest depth of focus, however in this region the intensity also drops down, which might increase the bias on S_4.

2.4 Birefringence

At last, the measured S_2 values can also be underestimated if the sample exhibits birefringence. Birefringence acts indeed as a distortion for excitation fields' polarization state, making them elliptic and tilted relative to their expected directions (3). Birefringence is known to be non-negligible in the myelin sheath, due to the tight and regular arrangement of lipids (4). We estimated the birefringence phase shift in myelin sample slices of thicknesses of about 30 μm in order to extrapolate the expected birefringence in the measured spinal cord tissues (Fig. S3). The slices were cut after extraction and fixation in the sagittal plane using a vibratome, and placed in phosphate-buffered saline (PBS).

The measurement of birefringence follows a method presented in (1, 5, 6) (Fig. S3). A laser beam ($\lambda = 800$ nm) is focused on the sample surface using the same microscope as used in PR-CARS. The incident linear polarization is rotated with an angle α (relative to the horizontal sample plane direction X) from $0°$ to $170°$ with a step of $10°$. The transmitted intensity modulation is recorded on a photomultiplier, placed after a polarizer of horizontal orientation (e.g. along the X direction of the sample plane, denoted (X, Y)). As a control in a non-birefringent sample, we performed the same experiment next to the spinal cord slice tissue in PBS. The resulting intensity polarization response along the X and Y analyzer directions can be written as quantities proportional to:

$$\begin{aligned} I_X(\alpha) &= |E_X(\alpha)|^2 \\ I_Y(\alpha) &= |E_Y(\alpha)|^2 \end{aligned}$$

where $E_{X,Y}$ are the transmitted field components along the X and Y directions respectively. Here only $I_X(\alpha)$ is measured. If birefringence occurs locally in a sample of given thickness, along a given optical axis direction Θ (typically the local direction of lipid chains in a thick multi-layer membrane), then the fields' components along this axis and its perpendicular direction will be phase-shifted by a value Φ. Before reaching the birefringent medium, the optical electric fields are written $(E_X, E_Y) = (\cos\alpha, \sin\alpha)$ in the laboratory frame. The birefringence imposes a phase shift Φ between the component of the

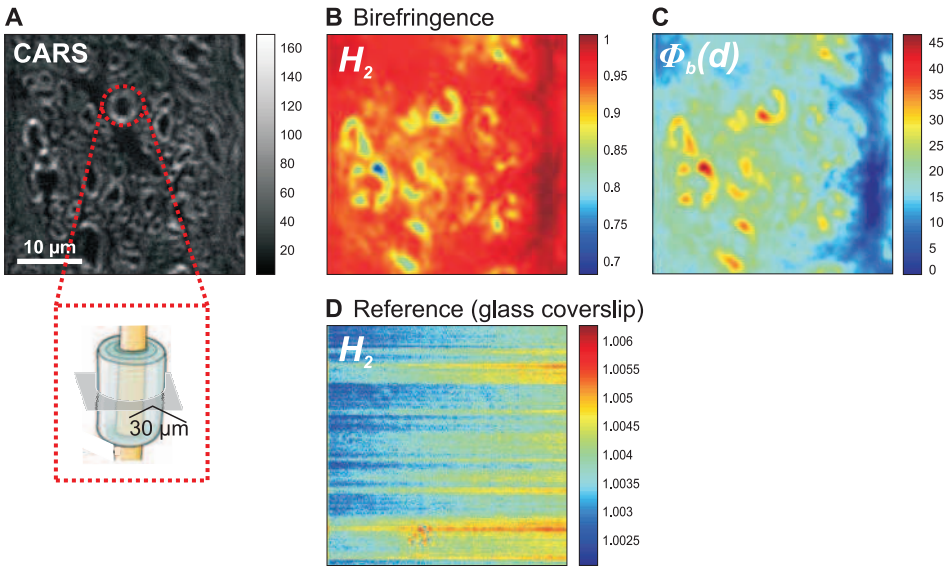

Figure S3: (***a***) CARS image (2845 cm^{-1}) of a spinal cord slice (mean thickness = 30 μm) on the region where the birefringence has been measured. (***b***) Measured H_2 map from the polarized signal measured on the spinal cord slice (in this scheme, values are not relevant for optical axes oriented along the horizontal and vertical orientations, see text). (***c***) Deduced birefringence Φ map of the deduced birefringence value. (***d***) Measured H_2 map from the signal measured on a glass coverslip.

field along the slow optical axis of the birefringent medium (denoted X_b) and its fast axis (denoted Y_b), such as:

$$\begin{aligned} E_{X_b}(\alpha,\Theta,\Phi) &= (\cos\alpha\,\cos\Theta+\sin\alpha\,\sin\Theta)\,e^{i\Phi} \\ E_{Y_b}(\alpha,\Theta,\Phi) &= (-\cos\alpha\,\sin\Theta+\sin\alpha\,\cos\Theta) \end{aligned}$$

Transforming this expression back in the sample plane frame (X,Y), the field components are written

$$\begin{aligned} E_X(\alpha,\Theta,\Phi) &= E_{X_b}(\alpha,\Theta,\Phi)\,\cos\Theta - E_{Y_b}(\alpha,\Theta,\Phi)\,\sin\Theta \\ E_Y(\alpha,\Theta,\Phi) &= E_{X_b}(\alpha,\Theta,\Phi)\,\sin\Theta + E_{Y_b}(\alpha,\Theta,\Phi)\,\cos\Theta \end{aligned}$$

The new intensity $I_X(\alpha,\Theta,\Phi)=|E_X(\alpha,\Theta,\Phi)|^2$ dependence can be easily decomposed into circular functions such as:

$$I_X(\alpha,\Theta,\Phi) = a_0(\Theta,\Phi)+a_2(\Theta,\Phi)\cos(2\alpha)+b_2(\Theta,\Phi)\sin(2\alpha) \quad (6)$$

with:

$$\begin{aligned} a_0(\Theta,\Phi) &= 1/2 \\ a_2(\Theta,\Phi) &= 1/2(1-\sin^2(2\Theta)(1-\cos\Phi)) \\ b_2(\Theta,\Phi) &= 1/4\sin(4\Theta)(1-\cos\Phi) \end{aligned}$$

We can define the magnitude and phase of this modulation as:

$$\begin{aligned} H_2(\Theta,\Phi) &= \tfrac{1}{a_0(\Theta,\Phi)}\sqrt{(a_2(\Theta,\Phi)^2+b_2(\Theta,\Phi)^2)} \\ \phi_2(\Theta,\Phi) &= 1/2\arctan(b_2(\Theta,\Phi)/a_2(\Theta,\Phi)) \end{aligned}$$

In an isotropic medium, the measured modulation is proportional to $\cos^2(\alpha)$, since there is no perturbation of the incident polarization state. The resulting expected values are thus $H_2 = 1$ and $\phi_2 = 0[\pi/2]$. In a birefringent sample $H_2=\sqrt{\cos^2(4\Theta)+\sin^2(4\Theta)\cos^2(\Phi)}$ and therefore H_2 is directly related to the birefringence phase shift Φ and the main birefringence axis direction Θ; it is generally lower than 1, except if $\Phi = 0[\pi]$, which means no birefringence, or a birefringence value which is an integer number of π. The fact that $H_2 \leq 1$ is due to the existence of ellipticity, induced by Φ. In order to extract the quantities (Φ,Θ) from the new measured modulation, some operations need to be performed on the modulation parameters (a_2,b_2):

$$\begin{aligned} \cos(\Phi) &= \arccos(1-\tfrac{2\,b_2}{\sin(4\Theta)}) \\ \tan(2\Theta) &= \tfrac{1-a_2}{b_2} \end{aligned}$$

The quantity Φ is thus extracted modulo π, while Θ is extracted modulo $\pi/2$. Note however that due to the measurement geometry (fixed analyzer axis), these quantities cannot be measured for $\Theta = 0[\pi/2]$. A rotation of the analyzer is necessary to disentangle this indetermination.

Values of H_2 calculated from the transmitted signal through the spinal cord sample are depicted in Fig. S3b. H_2 is clearly lower than 1 in many places of the sample, principally concentrated on the myelin sheath contours. The deduced phase shift Φ is shown in Fig. S3c. In this image, the birefringence can be quantified in regions of the myelin sheaths that do not correspond to orientations of the lipids around $0°$ or $90°$, for the reason indicated above.

The resulting Φ values range from $20°$ to $40°$for the 30 μm (on average) thick slice of the spinal cord sample, which indicates that the sample birefringence is quite large, as also previously reported in the literature. In comparison, the reference glass coverslip H_2 is very close to 1 as can be seen in Fig. S3d.

The found birefringence phase shift extrapolated for a depth of penetration of 30 μm (maximum focus depth used here) is therefore in the range of $20°$ to $40°$. The induced polarization distortions have been included in a model of the myelin sheath response (using input (S_2, S_4) values close to the measured ones), following the method described in (1). The birefringence values are seen to induce a negligible bias of (< 0.05) for S_2, and of 0.05 for S_4. Even though the myelin birefringence is non negligible, the shallow depth penetration used here allows neglecting this effect. However, it means that care has to be taken in case of future investigations at deeper penetration distances.

3 Molecular order in model lipid membranes

PR-CARS data were recorded in the spectral region averaged around the CH_2 symmetric stretching vibration. We considered MLVs having comparable intensity and size in the range from 5 to 30 μm, and imaged both "filled" and "non-filled" MLVs that were encountered in the samples (Fig. S4a, b).

In order to compare the organization of lipids in both populations, we considered only pixels taken from their border in the equatorial plane. (S_2, φ_2) images exhibit a strong orientational dependence of lipids in the equatorial plane of MLVs as compared to the isotropic aqueous solution, with CH bonds oriented along the membrane contour (Fig. S4c). The highest degree of the lipid order was found for non-filled MLVs made of DPPC lipids, with $\langle S_2 \rangle \approx 0.40$ and $\langle S_4 \rangle \approx 0.06$ (all averages are given over measurements performed over 5 to 10 MLVs). This corresponds to an effective distribution function resembling a Gaussian with an aperture $\sigma \approx 70°$ (Fig. S4d). Filled MLVs exhibit a higher disorder (Fig. S4d) ($\langle S_2 \rangle \approx 0.29$ and $\langle S_4 \rangle \approx 0.05$), most probably because of the lower tension exerted on the outer membranes due to the disorganized inner lipid layers. The measured order can change dramatically with different types of lipids, in particular their degree of saturation. Non-filled MLVs made of DOPC lipids exhibit a lower order with $\langle S_2 \rangle \approx 0.23$, with S_4 almost unchanged (Fig. S4e). This reflects the fact that at room temperature, DPPC is in the gel phase while DOPC is in the liquid disordered phase, with more possible conformational changes that leads to higher disorder (7).

4 Measurement of the g-ratio

The g-ratio is given by the ratio between the inner to the outer diameter of the myelin membrane (Fig. S5).

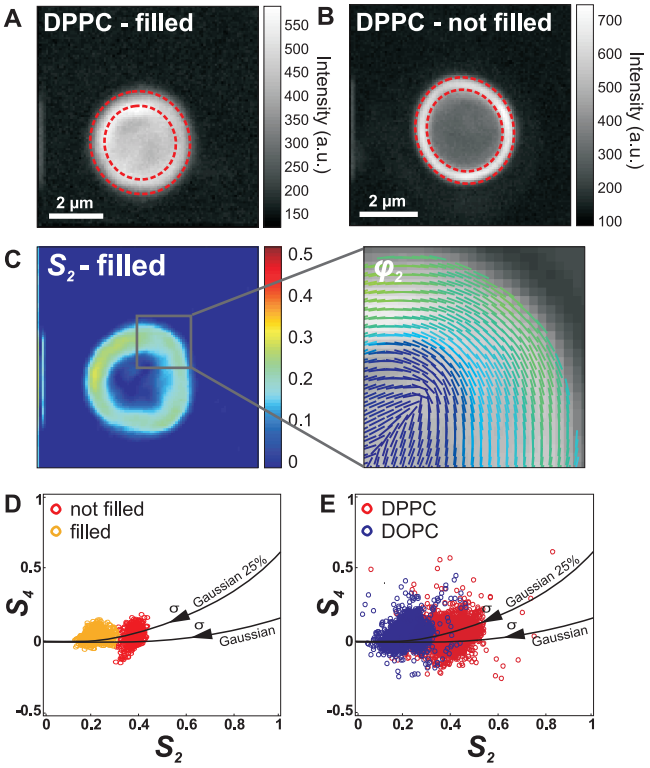

Figure S4: PR-CARS analysis on model multilamellar vesicles (MLVs) (around 2845 cm^{-1}). (***a***): intensity CARS image of the 'filled' MLVs made of pure DPPC. The dashed circles delimitate the region of analysis, emphasizing the outer edge of the MLV. (***b***) similar image for a 'not filled' DPPC MLV. (***c***) map of S_2 values (left) and corresponding φ_2 image showing the mean orientation of CH molecular bonds (right). (***d***) Comparison of (S_2, S_4) values in 'filled' and 'not filled' DPPC MLVs (each point is a pixel taken between dashed circles represented in the intensity images). (***e***) Comparison of (S_2, S_4) values in MLVs made of either pure DPPC or pure DOPC lipids. Continuous lines represent models from a pure Gaussian distribution and a Gaussian distribution superimposed with an isotropic distribution with a proportion of 25%.

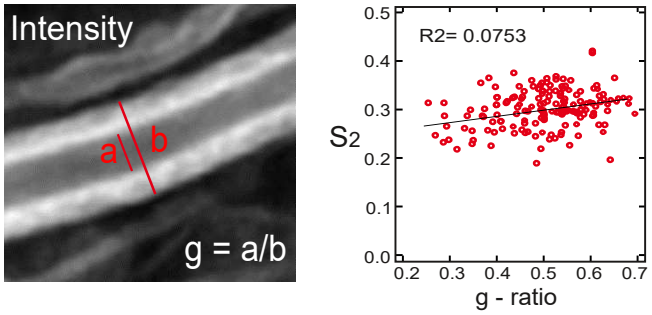

Figure S5: Measurement of the g-ratio in the equatorial plane of a myelin sheath, using the total intensity CARS image (a: inner diameter, b: outer diameter, g-ratio is the ratio between the inner and outer diameters). Mean $< S_2 >$ values of all measurements versus g-ratio on all , with linear interpolation and correlation coefficient of the fit.

5 Supporting References

References

1. Bioud, F. Z., and P. Gasecka, and P. Ferrand, and H. Rigneault, and J. Duboisset, and S. Brasselet. 2014. Structure of molecular packing probed by polarization-resolved nonlinear four-wave mixing and coherent anti-Stokes Raman-scattering microscopy. *Phys. Rev. A.*

89:013836–013846.
2. Duboisset, J., and P. Berto, and P. Gasecka, and F. Z. Bioud, and P. Ferrand, and H. Rigneault, and S. Brasselet. 2015. Molecular orientational order probed by coherent anti-Stokes Raman scattering (CARS) and stimulated Raman scattering (SRS) microscopy: A spectral comparative study. *J. Phys. Chem. B.* 119:3242–3249.
3. Munhoz, F., and S. Brustlein, and R. Hostein, and P. Berto, and S. Brasselet, and H. Rigneault. 2012. Polarization resolved stimulated raman scattering: probing depolarization ratios of liquids. *J. Raman Spectrosc.* 43:419–424.
4. De Campos Vidal, B., and M. L. S. Mello, and A. C. Caseiro-Filho, and C. Godo. 1980. Anisotropic properties of the myelin sheath. *Acta histochem.* 66:32–39.
5. Munhoz, F., and H. Rigneault, and S. Brasselet. 2010. High order symmetry structural properties of vibrational resonances using multiple-field polarization coherent anti-Stokes Raman spectroscopy microscopy. *Phys. Rev. Lett.* 105:123903–123907.
6. Aït-Belkacem, D., and A. Gasecka, and F. Munhoz, and S. Brustlein, and S. Brasselet. 2010. Influence of birefringence on polarization resolved nonlinear microscopy and collagen SHG structural imaging. *Opt. Express.* 18:14859–14870.
7. Heimburg, T. 2008. Thermal biophysics of membranes. Wiley-VCH, Berlin.

List of Figures